OPTIMIZATION OF ENERGY CONVERSION IN GOLD NANOPARTICLES IRRADIATED BY LIGHT FOR SUSTAINABLE ENERGY APPLICATION

Paweł Ziółkowski[1], Aimad Koulali[1*], Piotr Radomski[1*], Federica Zaccagnini[2], Iuliia Mukha[3], Francesca Petronella[4], Luciano De Sio[2], Dariusz Mikielewicz[1]

[1]Gdansk University of Technology, Faculty of Mechanical Engineering and Ship Technology, Institute of Energy, Gdansk, Pomerania, Poland

[2] Sapienza University of Rome, Department of Medico-Surgical Sciences and Biotechnologies, Latina, Lazio, Italy

[3]The National Academy of Science of Ukraine, Chuiko Insitute of Surface Chemistry, Kyiv, Kyiv Oblast, Ukraine

[4] National Research Council of Italy, Institute of Crystallography CNR-IC, Montelibretti, Lazio, Italy

*Corresponding Authors: aimad.koulali@pg.edu.pl; piotr.radomski@pg.edu.pl

ABSTRACT

This study investigates the optimization of light-to-heat conversion in gold nanoparticles under irradiation by continuous- and pulsed-wave laser sources. The conversion process relies on the absorption of electromagnetic energy and the subsequent generation of heat, a phenomenon that is integral to a variety of applications. The photothermal conversion model is based on the Rayleigh-Drude approximation, facilitating predictions of the optical cross-sections for capped gold nanorods. The mathematical model takes into account the shape and size parameters of the nanoparticles, in particular diameter and length, as well as the thickness of the capping agent, the concentration of the nanoparticles and the refractive indices of the surrounding medium and the capping material. The aim is to maximize the efficiency of photothermal conversion. Using the Nelder-Mead optimization algorithm, the research examines three distinct laser wavelengths: two continuous-wave lasers at 465 nm, 808 nm, and a pulsed laser at 532 nm, respectively. The present research extends to the mathematical modeling of six key parameters that influence the conversion of light to heat, providing a comprehensive optimization framework. The obtained results indicate that for continuous-wave lasers, the aspect ratio of optimal gold nanoparticle dimensions varies as a function of wavelength: a higher aspect ratio (0.7) is optimal for the shortest wavelength 465 nm, compared to the 808 nm wavelength with 0.17 aspect ratio. In contrast, for the pulsed laser at 532 nm, the aspect ratio of the optimal nanoparticles approaches almost unity (0.96), demonstrating that a quasi-spherical shape is most effective in maximizing heat generation. These results point to the dependence of photothermal efficiency on laser characteristics such as wavelength, pulse behavior and intensity. By correlating nanoparticle design with specific laser parameters, this work contributes to the targeted development of nanomaterials for efficient energy conversion in applications ranging from bacteria deactivation, through energy generation and medical therapies to materials processing.

1   INTRODUCTION

Gold nanoparticles (AuNPs) represent a well-known class of photoactive nanostructures that can be applied from power generation (De Sio *et al*., 2015), through bacteria deactivation (Petronella *et al*., 2022) to photothermal therapy (PTT) of cancer and other diseases (Hwang *et al*., 2014). Additionally, AuNPs-based phototherapeutic agents were demonstrated to produce efficient PTT effects both in vitro and in vivo (Vines *et al*., 2019). Due to the phenomenon of localized surface plasmon resonance (LSPR) (Pluchery, 2012), spherical AuNPs in colloidal suspensions display a specific red color that corresponds to a characteristic absorption band peaked at ~520-530 nm. A shift of AuNPs absorption allows utilization of near-infrared (NIR ~ 808 nm, or NIR-I) and shortwave infrared (SWIR or NIR-II;

~1000-2000nm) light for induction or enhancement of photothermal effects. NIR plasmonic absorbance can be achieved by using anisotropic gold nanoparticles (e.g., nanorods, nanocages, nanoshells, nanostars, etc. (Yuan *et al.*, 2012), or hybrid (composite) nanostructures that comprise gold with other materials (Zhang *et al.*, 2016). One more approach to increase the absorption of gold nanostructures in the NIR spectral region was shown by Mukha et al. (2021). The magnetic field induced aggregation of Fe_3O_4/Au magneto-plasmonic nanocomposites (MPNC) was accompanied by an increase in the absorption in NIR, which was demonstrated to provide an enhanced photothermal effect under NIR laser irradiation (at 808 nm).

In case of gold nanorods (AuNRs) absorption spectrum contains two LSPR bands. One band has small extinction in the visible region with a maximum located around 500-550nm (transverse band), and its position is independent on aspect ratio of nanorods. Another band belonging to the NIR spectral region is stronger (longitudinal band) and dominates the absorption spectra of AuNRs. The position of the longitudinal band maximum shifts with the increase of aspect ratio of AuNRs and the relationship between these parameters was defined in (Link *et al.*, 1999). Therefore, the aspect ratio of AuNPs can be used to precisely control the longitudinal band localization to meet the optical absorption requirements. As a result of the optimization of the length and diameter of the nanorods, a dedicated aspect ratio was obtained for specific wavelengths.

There are still scientific research debates on the best match for geometry for gold nanoparticles with rod-like structures for manifesting a better photothermal conversion effect. It has been reviewed that as the size of AuNRs decreases, the heat generation efficiency, blood retention, and intratumoral penetration could be improved. Additionally, smaller AuNRs also exhibited greater toxicity due to their high surface area compared to the mass and higher probability to interact with normal tissues. Therefore, smaller AuNRs, while showing better energy conversion efficiency, also increase the potential for toxic side effects (Ali *et al.*, 2019). However there are recent reviews on gold nanostructures for PTT use (Chuang *et al.*, 2022) and gold nanorods in particular (Liao *et al.*, 2021).

In addition to experimental investigation, theoretical research using models of physical phenomena occurring at the nanoscale should be conducted (Ziółkowski and Badur, 2018), and models should be used that allow optimization applying mathematical methods. The Nelder-Mead algorithm, developed by Nelder and Mead (1965), is distinguished as a robust, derivative-free optimization method ideally suited for complex, nonlinear optimization challenges where the gradient of the objective function remains elusive. This algorithm excels in its operation by manipulating a simplex—a geometric figure composed of $n + 1$ points within an n-dimensional space, where n signifies the quantity of parameters awaiting optimization (Luersen, and Le Riche, 2004). Such a method is invaluable for scenarios in which the objective function presents intricate dependencies on a multitude of parameters and the nonlinear dynamics characteristic of light-matter interactions. In recent contributions by Abdel-Basset et al. (2021), the utility and relevance of the Nelder-Mead algorithm has been highlighted by their ability to integrate it into modern multi-parameter optimization problems.

An additional advantage of the present approach is that it can be applied to hybrid optimization combining a deterministic aspect (Nelder-Mead method) with a stochastic one (e.g. Particle Swarm Optimization) (Ziółkowski *et al.*, 2021). However, it should be emphasized that the use of Nelder-Mead determines the direction of the analysis and allows the first recognition of the impact of a parameter change on the optimization process (Witanowski *et al.*, 2023).

The significance of the article topic lies in its potential to advance medical treatments, solar power generation and energy harvesting technologies. Optimized light-to-heat conversion allows for enhanced therapeutic outcomes in photothermal therapy, offering a promising avenue for improved cancer treatment. In the realm of energy harvesting, efficient energy conversion provides a pathway for harnessing and utilizing light energy, contributing to the development of sustainable and environmentally friendly energy solutions. The findings offer valuable insights for experimental setups, guiding researchers toward enhanced utilization of gold nanoparticles in diverse applications. The main aim of this study is to optimize the gold nanorods (ϕ, dCT, ds, dl, n_w and n_{CT}) using the Nelder-Mead

algorithm to achieve the highest heat generation rate of gold nanoparticles under laser irradiation. In turn, assessment for wavelength at $\lambda =$ 465 nm, $\lambda =$ 808 nm, and $\lambda =$ 532 nm and laser type is secondary objective. The wavelength is dictated by the capabilities of the manufacturers on the other hand, the nanoparticles are produced in many research centers and we have hope that it will be possible to produce them according to the results of optimization.

2 METHODOLOGY

The methodology first focuses on presenting the equations describing the conversion of electromagnetic energy into heat using gold nanowires, and secondly the optimization process is explored.

2.1 Energy conversion model

Solving the balance energy equation, the conversion rate can be described via a unified source term parameter which for semi-infinite systems, like thin films or platforms, is written by (Black, 2011; Radomski et al., 2021):

$$Se = \sigma_{abs} \cdot I_{abs} \tag{1}$$

where: σ_{abs} – absorption coefficient, m^{-1}; I_{abs} – intensity absorbed by the system, W·m^{-2}. This approach can be easily adopted for such a system where nanoparticles are deposited on a flat surface, treating them as inclusions in the semi-infinite region. Since only nanoparticles are capable of producing heat in the examined case, the heat generation rate from Equation 1, is substituted by Radomski et al. (2021; 2023a;b) and efficiency of photothermal process by Jiang *et al.*, (2013), as follows:

$$Se = \left(\xi \cdot (\eta_{PT} \cdot C_{ext})\right) \cdot I_0 \cdot (1 - R_{sys}) \cdot \left(1 - \exp\left(-(ds + 2 \cdot dCT) \cdot (\xi \cdot (\eta_{PT} \cdot C_{ext}))\right)\right) \tag{2}$$

$$\eta_{PT} = \frac{C_{abs}}{C_{ext}} = 1 - \frac{C_{sca}}{C_{ext}} \tag{3}$$

where: ξ – the number of nanoparticles per volume, m^{-3}; η_{PT} – photothermal efficiency, - ; C_{abs} – absorption cross section, m^2; C_{ext} – extinction cross section, m^2; C_{sca} – scattering cross section, m^2; I_0 – incoming intensity, W·m^{-2}; R_{sys} – reflected part of the system, - ; ds – short diameter of the nanoparticle, m; dCT – thickness of the capping agent, m.

The number of nanoparticles per volume can be related to the parameter ϕ that determines the distance between nanoparticles, which could be easily determined via electron microscopy techniques, and is assumed empirically by:

$$\xi = \frac{2}{(ds + 2 \cdot dCT + \phi)^2 \cdot (dl + 2 \cdot dCT + \phi)} \tag{4}$$

In this work, the Rayleigh-Drude approximation is employed to describe the optical cross-sections for the capped gold nanorods according to (Bohren and Huffman, 1983; Van de Hulst, 1981) :

$$C_{ext} = 4\pi \cdot \left(\frac{2\pi}{\lambda}\right) \cdot \mathbb{im}\left(\alpha_{\text{eff}}(ds, dl, dCT, n_w, n_{CT})\right) \tag{5}$$

$$C_{sca} = \left(\frac{8\pi}{3}\right) \cdot \left(\frac{2\pi}{\lambda}\right)^4 \cdot |\alpha_{\text{eff}}(ds, dl, dCT, n_w, n_{CT})|^2 \tag{6}$$

where: α_{eff} – effective polarizability from (Van de Hulst, 1981; Sihvola and Lindell, 1990), m^3 ; λ – incident wavelength, m; dl – length of the nanoparticle (long diameter), m ; n_w – refractive index of working medium, - ; n_{CT} – refractive index of the shell (capping agent), - .

The incoming light is assigned to have the round shape beam with a defined size, dB; and output power of light source, P_0, according to the formula:

$$I_0 = \frac{P_0}{\pi \cdot dB^2} \tag{7}$$

Moreover, the reflected part, R_{sys}, is established using the full Fresnel equations (Bohren and Huffman, 1983) on the adopted glass-sandwiched system with gold nanorods, which was previously examined in (Zaccagnini *et al*., 2023). For the pulsed laser, the intensity $I(t)$ depend on the time t, it can be described as fellows (Black, 2021):

$$I(t) = I_0 \cdot e^{\left(-4 \cdot \ln(2) \cdot \frac{t^2}{t_p^2}\right)} \tag{8}$$

This equation describes how the intensity of the laser pulse changes over time, assuming a Gaussian pulse shape, t is the time relative to the pulse peak, t_p and is the pulse duration, The factor $-4 \cdot \ln(2)$ ensures that the intensity decreases to half its maximum value (I_0) at the pulse duration's full width at half maximum (FWHM) (Black, 2021). The peak intensity of the laser at the beam's center (I_0), can be calculated using the following formula:

$$I_0 = \frac{P_{peak}}{\pi \cdot dB^2} \tag{9}$$

where P_{peak} is the peak power of the laser during a pulse by dividing the energy per pulse by the average pulse duration (Black, 2021). It can be calculated as function of the pulse duration t_p and the energy per pulse E:

$$P_{peak} = \frac{E}{t_p} \tag{10}$$

which refer to 1GHz frequency repetition rate, which is considered strictly for theoretical analysis.

2.2   Optimization procedure

The assumed objective in Nelder-Mead optimization procedure of this article is to maximizing heat generation which is influenced by a variety of physical parameters, including, but not limited to, the size and shape of the nanoparticles, the nature of the surrounding medium, the properties of the capping agent and the distances between nanoparticles. The following steps can describe the algorithm process, namely: 2.2.1 Initialization; 2.2.2 Evaluation and sorting; 2.2.3 Iteration steps; 2.2.4 Optimization process in Nelder-Mead method. However, it is necessary to define the objective function, which is determined as follows:

$$minimize\ (-Se) = minimize(-Se(\phi, dCT, ds, dl, n_w, n_{CT})) \tag{11}$$

2.2.1 Initialization: A simplex is formed with n vertices in the 6-dimensional parameter space, where (n) is the number of parameters. In this article it can be denoted each vertex as:

$$V_i = (\phi_i, dCT_i, ds_i, dl_i, n_{w_i}, n_{CT_i}) \tag{12}$$

where i from 1 to 7.
2.2.2 Evaluation and sorting: Each vertex V_i is evaluated by the function Se, resulting in 7 values representing the heat generation rate for each set of parameters. Next, the vertices are sorted according to their corresponding heat generation rates, from the highest (best) to the lowest (worst).

2.2.3 Iteration steps: Diagram of the Nelder-Mead algorithm applied in the present work is shown in Figure 1. Iteration steps are described below:

a) Reflection: the centroid c of the 6 better vertices (excluding the worst) is calculated. The algorithm reflects the worst vertex V_h across c to get a new point V_r taking into account reflection coefficient α as follows:

$$V_r = c + \alpha(c - V_h) \tag{13}$$

b) Decision on reflection: if $Se(V_r) > Se(V_h)$, V_h is replaced by V_r in the simplex.

c) Expansion: if $Se(V_r)$ is the highest in the simplex, which suggests that we are on a steeper slope towards the optimum, the algorithm attempts to take a larger step by expanding V_e

$$V_e = c + \gamma(V_r - c) \tag{14}$$

where γ is the expansion coefficient. If $Se(V_e) > Se(V_r)$, the simplex is updated by a simplex V_e.

d) Contraction: if $Se(V_r)$, fails to improve upon $Se(V_h)$, a contraction is performed between V_h and c to find V_c:

$$V_c = c + \omega(V_h - c) \tag{15}$$

where ω is the contraction coefficient. If $Se(V_c)$ improves upon $Se(V_h)$, V_h is replaced with V_c.

e) Shrinkage: if none of the above steps improve the worst heat generation rate, the algorithm performs a shrinkage, moving all vertices towards V_b, the vertex with the best heat generation rate.
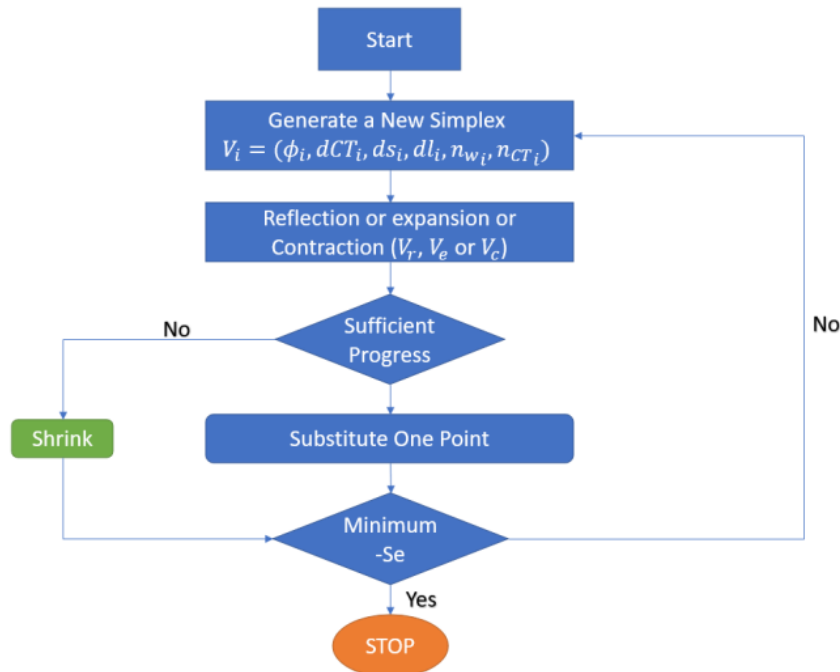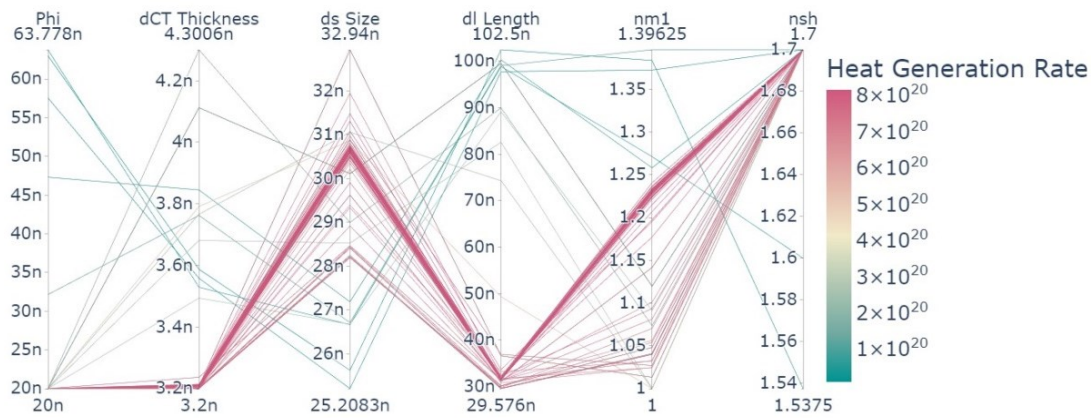

Figure 1: Diagram of the Nelder-Mead algorithm applied in the present work

2.2.4 To describe how the optimization process was conducted, we explore the parallel coordinates plot (see Figure 2), which represents a visualization of the multi-dimensional parameter space navigated by the Nelder-Mead algorithm. This plot demonstrates the variation and co-variation of six parameters: ϕ, dCT, ds, dl, n_w, and n_{CT}. Each polyline in this plot corresponds to a specific combination of these parameters, and the color indicates the heat generation rate that results from that combination, with warmer colors denoting higher rates. The spread of lines across the axes suggests the diversity of the

parameter sets evaluated during the optimization. The clustering of lines towards certain parameter values, particularly where the lines are redder, implies regions in the parameter space that correspond to higher heat generation rates, which are of primary interest.

Figure 2: Parallel coordinates plot for Nelder-Mead algorithm

The Figure 3 represents the optimization convergence plot, which tracks the improvement in the objective function—the heat generation rate—across the iterations of the Nelder-Mead algorithm. This plot shows a characteristic pattern of rapid initial improvement that tapers into a plateau, illustrating the convergence behavior typical of the Nelder-Mead process.

Initially, large leaps in heat generation rate state that the algorithm is quickly finding a better region of the parameter space. The subsequent leveling off of the curve indicates that the algorithm has reached a point of diminishing returns, where adjustments to the parameters no longer yield significant improvements, and suggests that an optimal or near-optimal solution has been found.
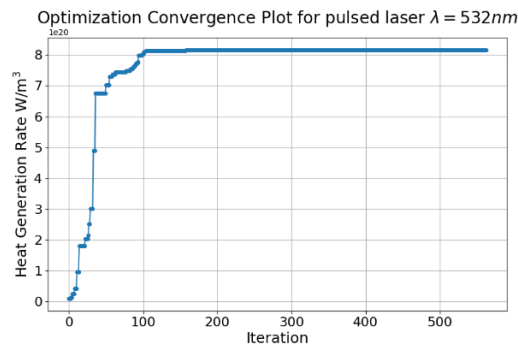
Figure 3: Optimization convergence plots for pulsed laser at $\lambda = 532$ nm.

3   RESULTS AND DISCUSSION

As mentioned earlier, optimization was conducted for parameters such as ϕ, dCT, ds, dl, n_w and n_{CT} in turn, assesment for wavelength at $\lambda = 465$ nm, $\lambda = 808$ nm, and $\lambda = 532$ nm and laser type.

3.1   Optimization result

The optimization results summarized in Table 1 show how the precise choice of nanoparticle size leads to significant improvements in photothermal conversion efficiency. The specific values for the diameters and lengths of gold nanoparticles (AuNPs) reveal the importance accorded to the interaction of laser light with these nanostructures. Note that the largest diameter and length optimized for λ=465 nm (39.75 nm and 57.09 nm respectively) are modified for wavelength λ=808 nm, with the diameter

decreasing to 12.59 nm while the length increases to 71.3 nm, suggesting a strongly wavelength-dependent optimization strategy. This wavelength-specific optimization refers to the results of Link and El-Sayed (2000), which highlighted the impact of particle size and shape on the resonance condition, stating that larger particle sizes for short-wavelength lasers optimize absorption and heat generation. The nearly spherical shape optimized for the 532 nm pulsed laser, giving a diameter of 30.06 nm, is in line with Gong *et al.* (2021), which demonstrated the effectiveness of spherical shapes in photothermal conversion due to their favorable surface plasmon resonance (SPR) properties.

Furthermore, with coating thickness and inter-particle distance consistently optimized at 3.2 nm and 20 nm for all wavelengths. This is also consistent with Gong *et al.* (2021), where intense laser pulses led to significant changes in the plasmon absorption, highlighting the influence of the environment and particle spacing on the thermal behavior of the nanoparticles. The refractive index of the surrounding medium and capping agent material varies with the laser wavelength, suggesting an adaptation to match the optical properties of the laser, which is a crucial factor in SPR tuning as detailed in (Chapagain *et al.*, 2021).

Table 1: Optimum parameters for wavelength (λ=465 nm, λ=808 nm, and λ=532 nm) and laser type (continuous-wavelength lasers and pulsed).

Parameter	Bounds	Continuous $\lambda = 465$ nm	Continuous $\lambda = 808$ nm	Continuous $\lambda = 532$nm	Pulsed laser $\lambda = 532$ nm
AuNPs diameter	$5 \leq ds \leq 50$ nm	39.75	12.59	29.00	30.06
AuNPs length	$5 \leq dl \leq 250$ nm	57.09	71.3	32.6	31.16
Capping agent thickness	$3.2 \leq dCT \leq 4$ nm	3.2	3.2	3.2	3.2
Distance between AuNPs	$20 \leq \phi \leq 150$ nm	20	20	20	20
Refractive index of surrounding medium	$1.0 \leq n_w \leq 1.7$	1.69	1.00	1.23	1.23
Refractive index of capping agent	$1.33 \leq n_{CT} \leq 1.7$	1.69	1.33	1.70	1.70
Maximum heat generated (W/m³)		**3.18×10^{13}**	**2.06×10^{14}**	**7.38×10^{13}**	**8.16×10^{20}**

Variations in heat generation for gold nanoparticles (AuNPs) optimized under different laser conditions highlight the interaction between laser characteristics and nanoparticle design to maximize photothermal efficiency. Continuous-wavelength lasers at $\lambda = 465 \, nm$ and $\lambda = 808 \, nm$ produce heat generations of 3.178×10^{13} W/m³ and 2.057×10^{14} W/m³, respectively. This variation reflects the tuning of nanoparticle dimensions to the unique interaction of each laser with matter (Chapagain *et al.*, 2021; Jain *et al.*, 2006), optimizing surface plasmon resonance (SPR) for efficient light absorption and heat conversion. The smaller optimal diameter for $\lambda = 808 \, nm$, at 12.59 nm, underlines the strategy of minimizing scattering and maximizing absorption, aligned with the deeper penetration of short infrared light that is crucial for enhanced photothermal conversion. In contrast, the pulsed laser at $\lambda = 532 \, nm$ significantly boosts heat generation at 8.161×10^{20} W/m³, highlighting the efficiency of near-spherical nanoparticles under the rapid, localized heating effects induced by pulsed lasers. This result aligns with the review of Au laser-NP interactions, highlighting the importance of fast processes induced by pulsed lasers to achieve nanoscale energy deposition via intensified light amplification and heat generation (Hashimoto *et al*., 2012). The marked difference between laser systems in terms of heat generation points to the importance of selecting appropriate nanoparticle geometries and laser settings for specific photothermal applications. Continuous-wave lasers provide a steady state of heating suitable for a wide range of therapeutic and materials processing applications. Furthermore, exceptional heat generation

under pulsed laser conditions reveals the potential for rapid, localized thermal effects, offering advantages in applications requiring rapid, intense heating, such as targeted cancer therapy, where it is essential to minimize damage to surrounding tissue (Hashimoto *et al.*, 2012).

3.2   Assessment description

3.2.1 Continues laser: In order to see the impact of each parameter individually on heat generation, heat generation diagrams have been presented in Figures 4 and 5.
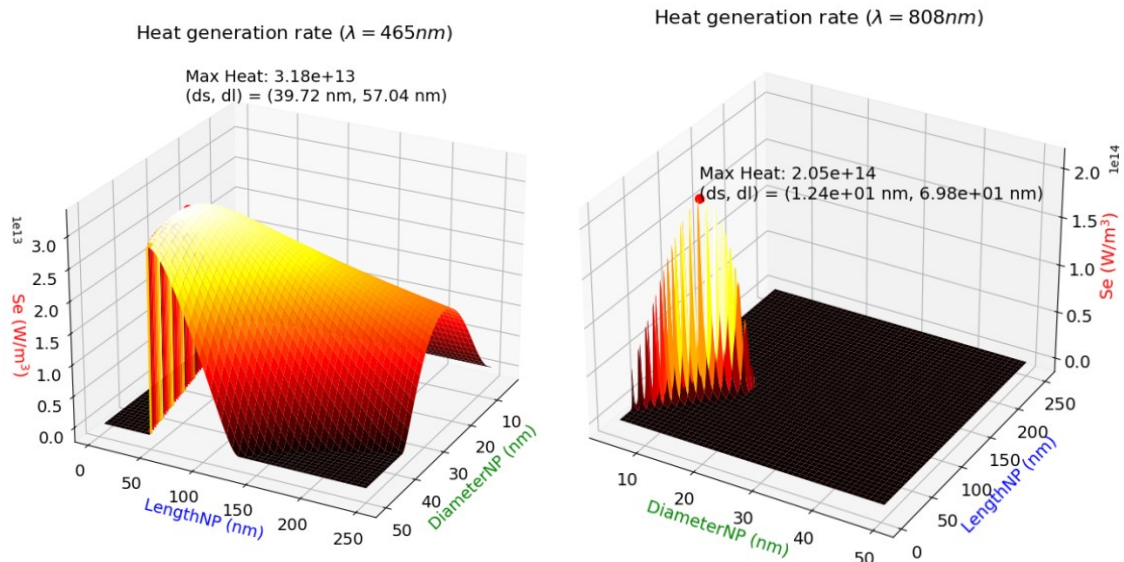
Figure 4: Assessment result, for $Se\,(ds, dl)$ using $\lambda = 465$ nm on the left and $\lambda = 808$ nm on the right, for fixed optimized parameter defined in Table.1
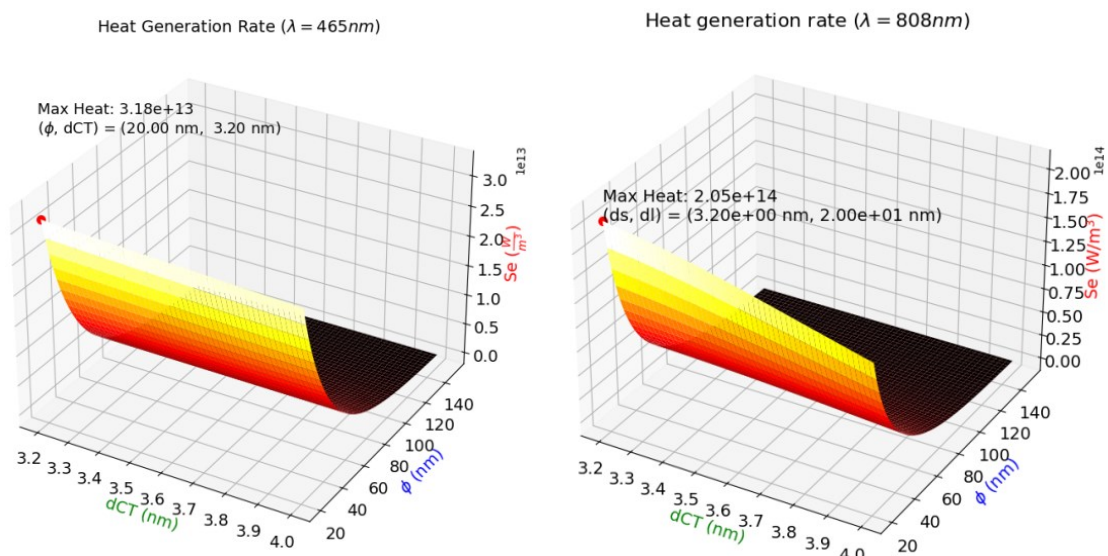
Figure 5: Assessment result, for $Se\,(\phi, dCT)$ using $\lambda = 465$ nm on the left and $\lambda = 808$ nm on the right, for fixed optimized parameter defined in Table 1

As shown in Figure 4, at a wavelength of 465 nm, the heat diagrams show a high and generalized heat generation rate for a variety of nanoparticle dimensions, implying that AuNPs with a wide range of aspect ratios are capable of efficient photothermal conversion. Specifically, the optimized parameters for this wavelength are a nanoparticle diameter of 39.7 nm and a length of 57 nm, resulting in an aspect ratio that facilitates a widespread spatial distribution of heat. It determines that at shorter wavelengths,

the photothermal conversion process can tolerate greater variability in nanoparticle size while maintaining high efficiency.

Conversely, at the longer wavelength of 808 nm (see Fig. 4), the optimal photothermal efficiency is achieved within a narrower range of nanoparticle dimensions, as indicated by the bright, sharply-defined region on the heat diagram. The optimal dimensions at this wavelength are a smaller nanoparticle diameter of 12.7 nm and a capping agent thickness of 3.2 nm. The high peak heat generation rate at these dimensions implies a more localized but intensely efficient photothermal effect, highlighting the necessity for precise tuning of nanoparticle sizes at this wavelength.

Comparing the aspect ratios of the optimal parameters at the two wavelengths, we see a significant difference. At 465 nm, a larger aspect ratio is optimal, while at 808 nm, a smaller diameter and longer length lead to a more elongated shape, suggesting that a different aspect ratio is needed for maximum heat generation. This elongated shape is likely due to the different interactions between laser light and the electronic properties of the nanoparticles at this particular wavelength. For the effects of capping agent thickness (dCT) combined with those of diameter (ds), using a laser ($\lambda = 465\ nm$), the large bright region across different diameters and capping agent thicknesses suggests that for this wavelength, a wider variety of nanoparticle sizes and capping thicknesses can generate heat efficiently. The second image ($\lambda = 808\ nm$) presents a very different scenario. The sharply defined bright region highlights the need for more precise nanoparticle sizes to achieve optimal heat generation.

Figure 5 includes the heat generation rates of gold nanorods subjected to laser irradiation at wavelengths of 465 nm and 808 nm, respectively. These diagrams show the relationships between nanorod length (dl), inter-nanorod distance (φ) - which is related to nanoparticle concentration - and coating thickness (dCT), against the background of a fixed set of parameters (ds, n_w, n_{CT}). The results reveal that optimal heat generation for the 465 nm wavelength occurs for a nanorod length of 57.0 nm and an inter-nanorod distance of 20.0 nm, with a capping agent thickness of 3.2 nm. Conversely, for the 808 nm wavelength, maximum efficiency is achieved with a longer nanorod length of 71.1 nm and the same inter-nanorod distance and capping agent thickness.

3.2.2 Pulsed laser: In Figure 6, which evaluates the photothermal efficiency of gold nanorods when subjected to a pulsed laser at a wavelength of 532, we observe two relationships: one reveals the variation of nanoparticle diameter with pulse time, and the other implies the change of nanoparticle length with pulse time. $1 \times \tau_p$ on the x-axis indicates the normalized duration of a single laser pulse, centered around the pulse's maximum intensity.
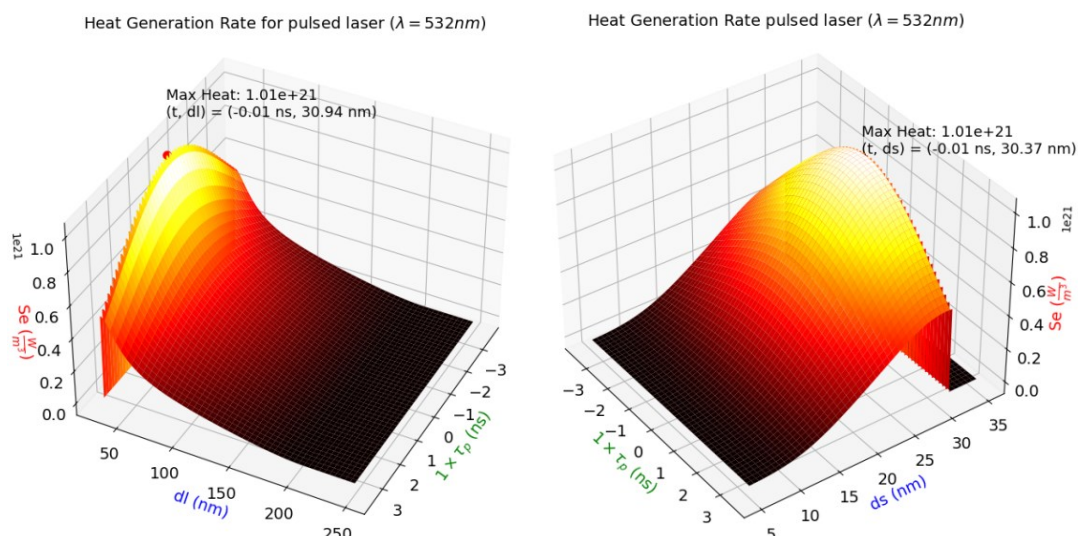
Figure 6: Assessment result, for Se (pulsed time, ds) and for Se (pulsed time, dl) using pulsed laser $\lambda = 532$ nm, for fixed optimized parameter defined in Table 1. (Zoom on 1 cycle pulsed time)

Figure 6 illustrates variations in the rate of heat generation over a single pulse duration, with the color gradient representing the intensity of heat generation. The graphs reveal that the rate of heat generation peaks at specific points in the pulse duration, corresponding to particular diameters and lengths of the nanoparticles. This suggests that the size and shape of nanoparticles can be optimized to maximize the conversion of laser energy into heat (see Figure 7), an essential aspect in many applications. These results highlight the dynamic nature of heat generation, pinpointing the exact moments within the laser pulse when energy absorption and, consequently, heat generation are at their peak. Crucially, the maximum heat generation rate observed in both curves reaches 1.01×10^{21} W/m^3 at the pulse peak, exceeding the expected maximum of 8.161×10^{20} W/m^3, as predicted by the optimization parameters detailed in Table 1. This discrepancy is explained by the fact that the first value represents an integrated measure of heat production over the entire pulse duration ($\tau_p = 7\,ns$), reflecting the overall efficiency of energy conversion throughout the cycle. In contrast, the second value, derived from both maps, reflects the instantaneous peak in heat production during the pulse cycle.
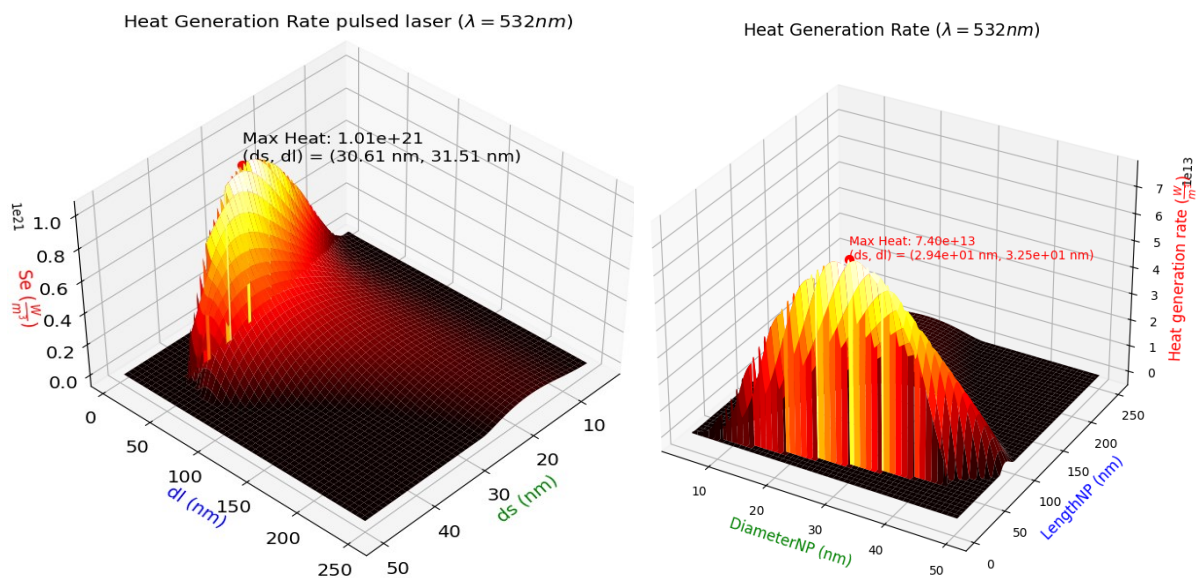
Figure 7: Assessment result, for $Se\,(ds, dl)$ at the peak time using pulsed laser (left) and continuous laser (right) $\lambda = 532$ nm, for fixed optimized parameter defined in Table 1.

4   CONCLUSIONS

This study has shown the complexity of the relationship between the geometric parameters of gold nanoparticles and their photothermal conversion efficiency under different laser irradiations. By applying the Nelder-Mead optimization algorithm, we identified the most efficient nanoparticle dimensions for three specific laser wavelengths.

For continuous-wave lasers, the results show a clear wavelength dependence of the optimum aspect ratio: shorter wavelengths ($\lambda = 465\,nm$) favor nanoparticles with a higher aspect ratio, while longer wavelengths ($\lambda = 808\,nm$) require a significantly lower aspect ratio for efficient heat generation. This contrast in aspect ratio indicates the role of resonant absorption and plasmonic efficiency at different wavelengths. It is interesting to note that for the pulsed laser at $\lambda = 532\,nm$, the results reveal an optimum aspect ratio close to unity, suggesting that near-spherical gold nanoparticles are most favorable for maximizing heat conversion at the wavelength. This corresponds to the transient heating effects presented only by pulsed lasers, which contrast with the continuous energy output of continuous-wave lasers. The higher heat generation with pulsed lasers compared to continuous lasers when irradiating gold nanoparticles, is primarily due to the higher peak power output of each pulse. These intense energy bursts allow gold nanoparticles to absorb more energy quickly, resulting in rapid and significant heat generation.

These results have significant implications for the design and application of gold nanoparticles in fields such as photothermal therapy, where customized heat output can significantly improve treatment effectiveness. Furthermore, in materials processing, where controlled heating is essential, the results of this study can serve as a basis for the synthesis of nanoparticles to achieve optimal energy conversion. Future work may explore the impact of additional parameters such as laser power density, pulse frequency and environmental conditions on photothermal efficiency.

REFERENCES

Abdel-Basset, M., Mohamed, R., Mirjalili, S., 2021, "A novel whale optimization algorithm integrated with Nelder–Mead simplex for multi-objective optimization problems," Knowl.-Based Syst., 212: 106619.

Ali, M. R. K., Wu, Y., El-Sayed, M. A., 2019, "Gold-nanoparticle-assisted plasmonic photothermal therapy advances toward clinical application," J. Phys. Chem. C, 123: 15375–15393.

Black, S.E., 2011, "Laser Ablation: Effects and Applications," Nova Science Publishers, New York, 276 p.

Bohren, C.F., Huffman, D.R., 1983, "Absorption and Scattering of Light by Small Particles," A Wiley-Interscience Publication, John Wiley & Sons, Toronto, 530 p.

Chapagain, P., Guisbiers, G., Kusper, M., Geoffrion, L. D., Benamara, M., Golden, A., Hewavitharana, L., 2021, "Tuning the Surface Plasmon Resonance of Gold Dumbbell Nanorods," ACS Omega, 6(10): 6871-6880.

De Sio, L., Placido, T., Comparelli, R., Curri, M. L., Striccoli, M., Tabiryan, N., Bunning, T. J., 2015, "Next-generation thermo-plasmonic technologies and plasmonic nanoparticles in optoelectronics," Prog. Quantum Electron., 41: 23.

Gong, B., Shen, Y., Li, H., Li, X., Huan, X., Zhou, J., Chen, Y., Wu, J., Li, W., 2021, "Thermo-Responsive Polymer Encapsulated Gold Nanorods for Single Continuous Wave Laser-Induced Photodynamic/Photothermal Tumour Therapy," J. Nanobiotechnol., 19(1): 1-4.

Hashimoto, S., Werner, D., Uwada, T., 2012, "Studies on the Interaction of Pulsed Lasers with Plasmonic Gold Nanoparticles Toward Light Manipulation, Heat Management, and Nanofabrication," J. Photochem. Photobiol. C: Photochem. Rev., 13(1): 28-54.

Hwang, S., Nam, J., Jung, S., Song, J., Doh, H., Kim, S., 2014, "Gold nanoparticle-mediated photothermal therapy: Current status and future perspective," Nanomedicine, 9: 2003–2022.

Jain, P.K., Lee, K.S., El-Sayed, I.H., El-Sayed, M.A., 2006, "Calculated Absorption and Scattering Properties of Gold Nanoparticles of Different Size, Shape, and Composition: Applications in Biological Imaging and Biomedicine," J. Phys. Chem. B, 110(14): 7238-7248.

Jiang, K., Smith, D.A., Pinchuk, A., 2013, "Size-Dependent Photothermal Conversion Efficiency of Plasmonically Heated Gold Nanoparticles," J. Phys. Chem. C, 117: 27073-27080.

Link, S., El-Sayed, M. A., 2000, "Shape and Size Dependence of Radiative, Non-Radiative and Photothermal Properties of Gold Nanocrystals," Int. Rev. Phys. Chem., 19(3): 409-453.

Link, S., Mohamed, M.B., El-Sayed, M. A., 1999, "Simulation of the Optical Absorption Spectra of Gold Nanorods as a Function of Their Aspect Ratio and the Effect of the Medium Dielectric Constant," J. Phys. Chem. B, 103(16): 3073-3077.

Luersen, M.A., Le Riche, R., 2004, "Globalized Nelder–Mead method for engineering optimization," Comput. Struct., 82(23-26): 2251-2260.

Mukha, I., Chepurna, O., Vityuk, N., Khodko, A., Storozhuk, L., Dzhagan, V., Zahn, D.R.T., Ntziachristos, V., Chmyrov, A., Ohulchanskyy, T.Y., 2021, "Multifunctional Magneto-Plasmonic Fe3O4/Au Nanocomposites: Approaching Magnetophoretically Enhanced Photothermal Therapy," Nanomaterials, 11: 1113.

Nelder, J.A., Mead, R., 1965, "A simplex method for function minimization," The Comput. J., 7(4): 308-313.

Petronella, F., De Biase, D., Zaccagnini, F., Verrina, V., Lim, S., Jeong, K., Miglietta, S., Petrozza, V., Scognamiglio, V., Godman, N.P., Evans, D.R., McConney, M., De Sio, L., 2022, "Label-free and

reusable antibody-functionalized gold nanorod arrays for the rapid detection of Escherichia coli cells in a water dispersion," Environ. Sci. Nano, 9: 3343-3360.

Pluchery, O., 2012, "Optical Properties of Gold Nanoparticles," In: Louis, C., Pluchery, O. (eds), Gold Nanoparticles for Physics, Chemistry, and Biology, Imperial College Press, London, UK: 87-114.

Radomski, P., Ziółkowski, P., De Sio, L., Mikielewicz, D., 2021, "Computational fluid dynamics simulation of heat transfer from densely packed gold nanoparticles to isotropic media," Arch. Thermodyn., 42(3): 87-114.

Radomski, P., Zaccagnini, F., Ziółkowski, P., Petronella, F., De Sio, L., Mikielewicz, D., 2023a, "Heat Transfer of the Multicolor-Laser-Sources-Irradiated Nanoparticles in Reference to Thermal Processes," Proc. 36th Int. Conf. on Efficiency, Cost, Optimization, Simulation and Environmental Impact on Energy Systems, ECOS 2023: 356-367.

Radomski, P., Ziółkowski, P., Mikielewicz, D., 2023b, "Energy conversion in systems-contained laser irradiated metallic nanoparticles - comparison of results from analytical solutions and numerical methods," Acta Mech. et Autom., 14(4): 540-549.

Sihvola, A., Lindell, I.V., 1990, "Polarizability and Effective Permittivity of Layered and Continuously Inhomogeneous Dielectric Ellipsoids," J. Electromagn. Waves Appl., 4(1): 1-26.

Van de Hulst, H.C., 1981, "Light Scattering by Small Particles," Dover Publications, Inc., New York, 470 p.

Vines, J.B., Yoon, J.-H., Ryu, N.-E., Lim, D.-J., Park, H., 2019, "Gold Nanoparticles for Photothermal Cancer Therapy," Front. Chem., 7: 167.

Witanowski, Ł., Ziółkowski, P., Klonowicz, P., Lampart, P., 2023, "A hybrid approach to optimization of radial inflow turbine with principal component analysis," Energy, vol. 272, 127064.

Yuan, H., Fales, A.M., Vo-Dinh, T., 2012, "TAT Peptide-Functionalized Gold Nanostars: Enhanced Intracellular Delivery and Efficient NIR Photothermal Therapy Using Ultralow Irradiance," J. Am. Chem. Soc., 134: 11358–11361.

Zaccagnini, F., Radomski, P., Sforza, M.L., Ziółkowski, P., Lim, S. I., Jeong, K.U., Mikielewicz, D., Godman, N.P., Evans, D.R., Slagle, J.E., McConney, M.E., De Biase, D., Petronella, F., De Sio, L., 2023, "White light thermoplasmonic activated gold nanorod arrays enable the photo-thermal disinfection of medical tools from bacterial contamination," J. Mater. Chem. B, vol. 11(1): 6823 – 6836.

Zhang, L., Chen, Y., Li, Z., Li, L., Saint-Cricq, P., Li, C., Lin, J., Wang, C., Su, Z., Zink, J.I., 2016, "Tailored Synthesis of Octopus-type Janus Nanoparticles for Synergistic Actively Targeted and Chemo-Photothermal Therapy," Angew. Chem. Int. Ed., 55: 2118–2121.

Ziółkowski, P., Badur, J., 2018, "A theoretical, numerical and experimental verification of the Reynolds thermal transpiration law," Int. J. Numer. Methods Heat Fluid Flow, 28(1): 1.

Ziółkowski, P., Witanowski, Ł., Klonowicz, P., Głuch, S., 2021, "Optimization of the last stage of gas-steam turbine using a hybrid method," 14th Eur. Conf. on Turbomachinery Fluid Dynamics and Thermodynamics, 12-16 April, Online, Gdańsk: Code 176576.

ACKNOWLEDGEMENTS